Modeling and inversion of 1-D profiles in time-domain

Mehbub-ur Rahman and René Marklein
Department of Electrical Engineering and Computer Science, University of Kassel, Kassel, Germany

Abstract

Purpose – The purpose of this paper is to present a time-domain technique to compute the electromagnetic wave field and to reconstruct the permittivity and electric conductivity profile of a one-dimensional slab of finite length.

Design/methodology/approach – The forward scattering problem is solved by a Green's function formulation to generate synthetic data that are used as a testbed for the inversion scheme. The inverse scattering problem is solved by reconstructing the unknown permittivity and electric conductivity profile of the medium with the help of an invariant embedding method.

Findings – The Green's operator maps the incident field on either side of the medium to the field at an arbitrary observation point inside the slab and hence, the internal fields can be computed directly without computing the wave field throughout the entire medium. The invariant embedding method requires a finite time trace of reflection data and therefore it is suitable for reconstructing the material parameters in real-time.

Practical implications – The implemented methods have been validated against synthetic and measured time domain reflectometry data.

Originality/value – This paper fulfils an identified need to determine unknown one-dimensional profiles and thus plays an important role in electromagnetics, non-destructive testing, and geophysics.

Keywords Waves, Electromagnetism, Non-destructive testing, Geophysics

Paper type Research paper

I. Introduction

Recently, 1-D profiling has become a point of high interest, for instance in geophysics and non-destructive testing (NDT), not only due to the ease to solve the problems analytically but also due to a high-accuracy level. It has great importance in the time domain reflectometry such as moisture meter and material analysis (Connor and Dowding, 1999; Schlaeger, 2002). The forward solver of such schemes works on a known slab and determines the electromagnetic field. On the other hand, the inverse solver takes the reflection data from the slab as an input and determines the properties of the unknown slab. The known methods to solve the forward problem are for instance:

- finite-difference time-domain method (Taflove and Hagness, 2000);
- finite integration technique (Weiland, 1977; Marklein, 2002);
- finite element method (Jin, 2002); and
- Green's function approach (Krueger and Ochs Jr, 1989; Rahman and Marklein, 2005).

The authors would like to thank Christiane Maierhofer from the Federal Institute for Materials Research and Testing (BAM, Germany) for the provided measurement datasets.

COMPEL: The International Journal for Computation and Mathematics in Electrical and Electronic Engineering
Vol. 28 No. 5, 2009
pp. 1349-1361

0332-1649
DOI 10.1108/03321640910969584

The Green's function approach has some advantages over the other methods. First, in this method the wave equation needs not to be solved for each incident wave form. Second, the wave field throughout the entire medium does not have to be computed. For these advantages, this method has been implemented in the forward solver.

The inverse problem can be solved by:

- invariant embedding (Corones *et al.*, 1983; Kristensson and Krueger, 1992); and
- downward continuation (Kristensson and Krueger, 1986).

The less amount of input data could be mentioned as main advantage of the layer stripping method. Obviously, the reflection data should be processed before feeding them into the inverse scheme.

II. Statement of the problem

The geometry of the problem is shown in Figure 1. An inhomogeneous slab occupies the region $0 \leq z \leq L$. The permittivity and conductivity profiles are functions of depth z only.

A homogeneous, lossless medium is situated on either side of the slab. The electric field strength $E(z, t)$ within the slab can be expressed by:

$$\frac{\partial^2}{\partial z^2} E(z,t) - \frac{1}{c^2(z)} \frac{\partial^2}{\partial t^2} E(z,t) - b(z) \frac{\partial}{\partial t} E(z,t) = 0, \tag{1}$$

where:

$$c^{-2}(z) = \varepsilon(z)\mu_0, \quad b(z) = \sigma_{\rho e}(z)\mu_0. \tag{2}$$

Here, μ_0, $\sigma_e(z)$ and $\varepsilon(z)$ represent the permeability of vacuum, electric conductivity and permittivity, respectively. The phase velocity $c(z)$ is assumed to be continuous at the boundary, which means:

$$c(z) = c(0^+), \ z \leq 0; \quad c(z) = c(L^-), \ z \geq L. \tag{3}$$

III. Normalization of the wave equation

In order to facilitate, the numerical computations a conversion to travel time coordinates is made. These coordinates are defined as:

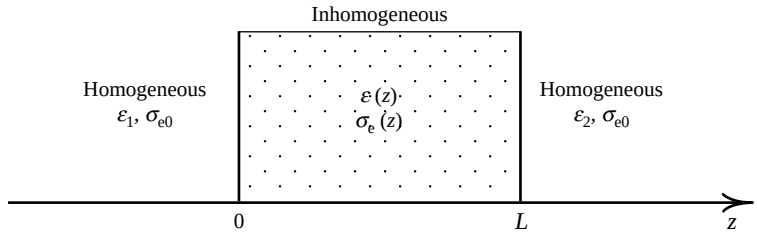

Figure 1.
Geometry of the inhomogeneous slab; medium 1: ε_1, σ_{e0}; slab: $\varepsilon(z)$, $\sigma_e(z)$; medium 2: ε_2, σ_{e0}

$$l = \int_0^L \frac{1}{c(z)}\,\mathrm{d}z, \quad s(t) = \frac{t}{l} \tag{4}$$

$$x = x(z) = \int_{z'=0}^{z} \frac{1}{lc(z')}\,\mathrm{d}z', \quad u(x,s) = E(z,t), \tag{5}$$

where x is the normalized distance and s is the normalized time. The slab occupies the region $0 \leq x \leq 1$ and a round trip time is described by $0 < s < 2$ which is equivalent to $2l$. In fact, l represents the time taken by the wave front to travel through the slab once. So the wave equation will be transformed into:

$$\frac{\partial^2}{\partial x^2}u(x,s) - \frac{\partial^2}{\partial s^2}u(x,s) + A(x)\frac{\partial}{\partial x}u(x,s) + B(x)\frac{\partial}{\partial s}u(x,s) = 0\,, \tag{6}$$

where:

$$A(x) = -\frac{\mathrm{d}}{\mathrm{d}x}\ln\ c[z(x)] \tag{7}$$

$$B(x) = -lb[z(x)]\ \ c^2[z(x)]. \tag{8}$$

IV. Wave splitting

The wave travelling in the non-homogeneous slab can be splitted into left- and right-going parts.

In Figure 2, $u^+(x, s)$ is the right going wave and $u^-(x, s)$ is the left going wave. For all time s, the initial and boundary conditions are:

$$u^+(x,0) = u^-(x,0) = 0; \quad 0 < x < 1 \tag{9}$$

$$u^+(0,s) = f(s), \ \ u^-(1,s) = 0; \quad s > 0. \tag{10}$$

An incident wave, impinged only from the left side, is denoted by $f(s)$.

V. Forward solver: Green's function approach

The Green's function approach is applied to model the forward problem. We assume that the incident wave, the length of the slab L, the relative permittivity ε_r, and the electric conductivity σ_e profile are known. The goal is to determine the internal wave field. A matrix operator $[\mathbf{G}](x)$ can be defined to map the incident waves $u^+(0, s)$ and $u^-(1, s)$ to internal fields $u^+(x, s)$ and $u^-(x, s)$ as:

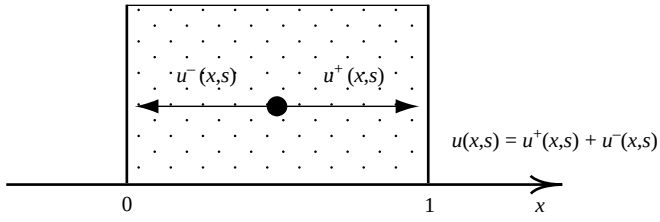

Figure 2.
Wave splitting; $u^+(x, s)$: right going wave and $u^-(x, s)$: left going wave

$$\begin{Bmatrix} u^+(x,s) \\ u^-(x,s) \end{Bmatrix} = \underbrace{\begin{bmatrix} G_{11}(x) & G_{12}(x) \\ G_{21}(x) & G_{22}(x) \end{bmatrix}}_{=[G](x)} \begin{Bmatrix} u^+(0,s) \\ u^-(1,s) \end{Bmatrix}. \tag{11}$$

Considering an incident wave only from left side, we find:

$$\left.\begin{aligned} u^+(x,s) &= G_{11}(x)*f(s) \\ u^-(x,s) &= G_{21}(x)*f(s) \end{aligned}\right\}; \quad \text{as } u^+(0,s) = f(s), \tag{12}$$

where "*" denotes convolution. G_{11} and G_{21} are related to the forward and backward travelling wave, respectively, when the incident wave is applied from the left side of the slab. G_{12} and G_{22}, are not considered here as they are only applicable for an incident wave coming from the right side of the slab. Now by applying Duhamel's integral:

$$u^+(x,s) = t^+(0,x)\left\{ f(s-x)\int_0^{s-x} f(s')G_{11}(x,s-s')\mathrm{d}s' \right\} \tag{13}$$

$$u^-(x,s) = \frac{1}{t^-(0,x)}\int_0^{s-x} f(s')G_{21}(x,s-s')\mathrm{d}s', \tag{14}$$

where:

$$t^{\pm}(x_1,x_2) = \exp\left\{ \pm\frac{1}{2}\int_{x1}^{x2} [A(x'] \mp B(x')]\mathrm{d}x' \right\}. \tag{15}$$

VI. Equations of the Green's Kernel

The fields $u^+(x,s)$ and $u^-(x,s)$ satisfy the following equation:

$$\frac{\partial}{\partial x}\begin{Bmatrix} u^+(x,s) \\ u^-(x,s) \end{Bmatrix} = \begin{bmatrix} \alpha(x) & \beta(x) \\ \gamma(x) & \delta(x) \end{bmatrix} \begin{Bmatrix} u^+(x,s) \\ u^-(x,s) \end{Bmatrix}, \tag{16}$$

where $\alpha(x)$, $\beta(x)$, $\gamma(x)$, and $\delta(x)$ are the functions of $A(x)$, $B(x)$ and incorporate time derivative $\partial/\partial s$. From equations (11) and (16), it can be summarized that:

$$\frac{\partial}{\partial x}[\mathbf{G}](x) = \begin{bmatrix} \alpha(x) & \beta(x) \\ \gamma(x) & \delta(x) \end{bmatrix} \begin{bmatrix} G_{11}(x) & G_{12}(x) \\ G_{21}(x) & G_{22}(x) \end{bmatrix}. \tag{17}$$

Again using equation (12), it can be shown that:

$$\frac{\partial}{\partial x}[G_{11}(x)f](s) = \alpha(x)[G_{11}(x)f](s) + \beta(x)[G_{21}(x)f](s). \tag{18}$$

Substituting $[G_{11}(x)f](s)$ by the right side of equation (13), a simple expression of G_{11} can be obtained as follows:

$$\frac{\partial}{\partial x}G_{11}(x,s) + \frac{\partial}{\partial s}G_{11}(x,s) = \frac{1}{2}[A(x)+B(x)]\exp\left\{ -\int_0^x B(x')\mathrm{d}x' \right\} G_{21}(x,s). \tag{19}$$

Similarly using equation (14), G_{21} can be defined as:

$$\frac{\partial}{\partial x} G_{21}(x,s) + \frac{\partial}{\partial s} G_{21}(x,s) = \frac{1}{2}[A(x) - B(x)]\exp\left\{\int_0^x B(x')\mathrm{d}x'\right\} G_{11}(x,s). \quad (20)$$

G_{11} is continuous everywhere except on $s = x$ (Figure 3). On this line the kernels can be expressed as:

$$G_{11}(x,x^+) = -\frac{1}{8}\int_0^x [A^2(x') - B^2(x')]\mathrm{d}x' \quad (21)$$

$$G_{21}(x,x^+) = -\frac{1}{4}[A(x) - B(x)]\exp\left\{\int_0^x B(x')\mathrm{d}x'\right\}. \quad (22)$$

Again on the line $s = 2 - x$:

$$G_{21}(x,(2-x)^+) - G_{21}(x,(2-x)^-) = \frac{1}{4}[A(1) - B(1)]\exp\left\{\int_0^1 B(x')\mathrm{d}x'\right\}. \quad (23)$$

The initial and boundary conditions can be defined as:

$$G_{11}(x,s) = G_{21}(x,s) = 0; \quad s < x \quad (24)$$

$$G_{11}(0,s) = G_{21}(1,s) = 0; \quad s > 0. \quad (25)$$

VII. Numerical implementation of the forward solver

The Green's kernels explained by equations (19) and (20) can also be implemented numerically. By fixing a constant Δ, the first equation can be integrated from $(x - \Delta, s - \Delta)$ to (x, s) along the characteristics $s - x = \text{const.}$ and the second one from (x, s) to $(x + \Delta, s - \Delta)$ along the characteristics $s + x = \text{const.}$ with approximating the right-hand side by the trapezoidal rule. So the equations will become:

$$G_{11}(x,s) - G_{11}(x-\Delta,s-\Delta) = a(x)G_{21}(x,s) + a(x-\Delta)G_{21}(x-\Delta,s-\Delta) + O(\Delta^3) \quad (26)$$

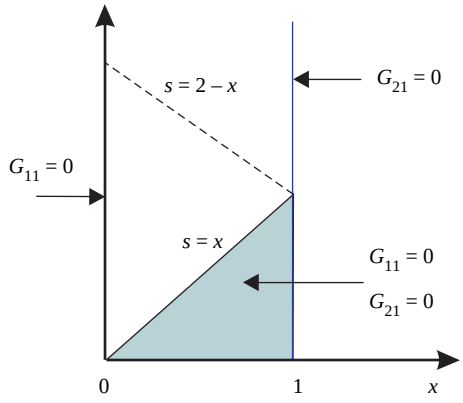

Figure 3.
Conditions of the Green's kernel

$$G_{21}(x+\Delta, s-\Delta) - G_{21}(x,s) = b(x)G_{11}(x,s) + b(x+\Delta)G_{11}(x+\Delta, s-\Delta) + O(\Delta^3), \quad (27)$$

where:

$$a(x) = \frac{1}{4}\Delta[A(x) + B(x)]\exp\left(-\int_{x'=0}^{x} B(x')\mathrm{d}x'\right) \quad (28)$$

$$b(x) = \frac{1}{4}\Delta[A(x) - B(x)]\exp\left(\int_{x'=0}^{x} B(x')\mathrm{d}x'\right). \quad (29)$$

Let us now introduce a grid of points as shown in Figure 4: $(x_i, s_{i+2j}) = (i\Delta, (i+2j)\Delta)$, $i = 0, \ldots, N; j = 0, \ldots$ Here N represents the total number of grid points. Considering $\Delta = 1/N$, it can be stated that:

$$G_{11}^{i,j} = G_{11}(i\Delta, (i+2j)\Delta), \quad a^i = a(i\Delta) \quad (30)$$

$$G_{21}^{i,j} = G_{21}(i\Delta, (i+2j)\Delta), \quad b^i = b(i\Delta). \quad (31)$$

Using these approximations, equations (26) and (27) can be rewritten as:

$$G_{11}^{i,j} = d^i\left[G_{11}^{i-1,j} + a^{i-1}G_{21}^{i-1,j} - a^i b^{i+1}G_{11}^{i+1,j-1} + a^i G_{21}^{i+1,j-1}\right] \quad (32)$$

$$G_{21}^{i,j} = d^i\left[-b^i G_{11}^{i-1,j} - a^{i-1}b^i G_{21}^{i-1,j} - b^{i+1}G_{11}^{i+1,j-1} + G_{21}^{i+1,j-1}\right], \quad (33)$$

where:

$$d^i = [1 + a^i b^i]^{-1} = \left[1 + \frac{1}{16}\Delta^2(A^2(i\Delta) - B^2(i\Delta))\right]^{-1} \quad (34)$$

and $i = 1, 2 \ldots, N-1; j = 1, 2, \ldots$ The initial condition represented by $s = x$, i.e. $j = 0$, can be determined by equations (21) and (22). The boundary conditions are:

$$G_{11}^{0,j} = 0, \quad G_{21}^{N,j} = 0; \quad j = 0, 1, 2, \ldots \quad (35)$$

To incorporate the discontinuity of G_{21} on the line $s = 2 - x$, i.e. $j = N - i$, $G_{21}^{i,N-i}$ below the line can be computed by equation (31). Above this line, $(G_{21}^{i,N-i})^+$ can be determined by:

$$\left(G_{21}^{i,N-i}\right) = \left(G_{21}^{i,N-i}\right)^- + \frac{1}{4}[A(1) - B(1)]\exp\int_0^1 B(x)\mathrm{d}x. \quad (36)$$

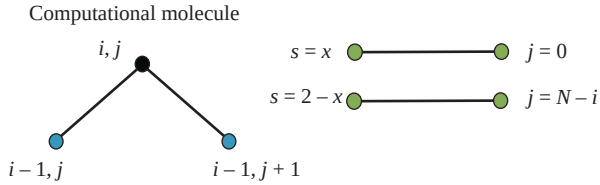

Figure 4.
Computational molecule and variable transformation

This value is used in place of $G_{21}^{i,N-i}$ determined by equation (33) while computing $G_{11}^{i,N-i+1}$ and $G_{21}^{i,N-i+1}$.

VIII. Software implementation of the forward solver

This scheme has already been tested to simulate sinusoidal, square, and multiple Gaussian shaped ε_r profiles. Considered electromagnetic pulses are: Dirac pulse, Gaussian pulse, five pulses of a sinusoidal wave, raised cosine, and step function. The results have been tested in both lossless and lossy condition. As an example we consider the material profile of a floor model as shown in Figure 5, which has been constructed by the Fraunhofer Institute for NDT (IZFP, Saarbrücken, Germany).The left side of the test specimen is illuminated by a broadband raised cosine pulse with two cycles and a carrier frequency of 1.68 GHz. The computed electromagnetic wave field is shown in Figure 6.

A multiple Gaussian shaped slab model with incident Gaussian pulse has been simulated as the second example (Figures 7 and 8).

IX. Inverse solver: invariant embedding method

The inverse problem is solved by the invariant embedding (also known as layer–stripping) method (Rahman and Marklein, 2005), originally suggested in (Kristensson and Krueger, 1992). This algorithm determines the unknown relative permittivity profile ε_r of the slab from the known values, like slab length L, incident

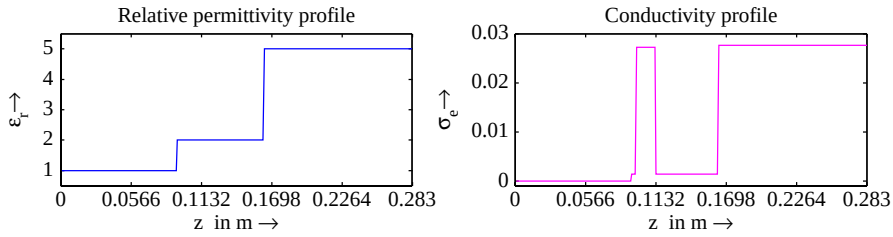

Notes: Parameter: L = 28.3 cm, $N_z = N_x$ = 304, Δ = 931 μm, Δt = 5 ps

Figure 5.
Profiles of a floor model: ε_r (left) and σ_e (right) profile

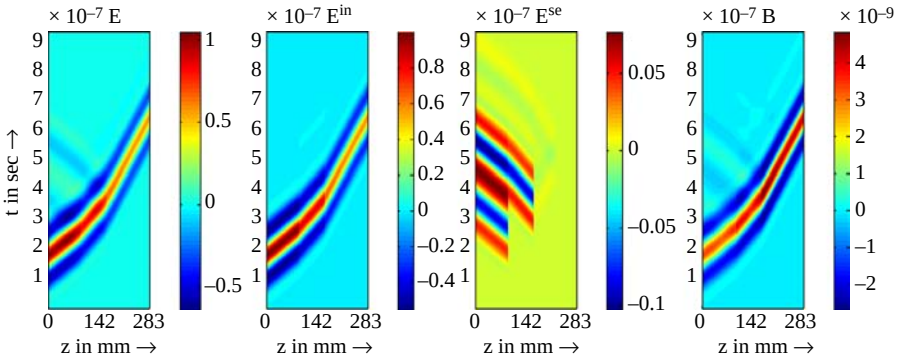

Notes: Parameter: L = 28.3 cm, $N_z = N_x$ = 304, Δ = 931 μm, Δt = 5 ps

Figure 6.
Computed wave field: E: total, E^{in}: incident, and E^{sc}: scattered electric field strength as well as B: magnetic flux density

pulse, relative permittivity of the first medium $\varepsilon_r^{(1)}$, and computed or measured reflection data. From the wave splitting phenomenon, it can be shown that:

$$E(z,t) = E^+(z,t) + E^-(z,t). \tag{37}$$

The backward travelling wave $E^-(z, t)$ can be associated with reflection kernel $R^+(z, t)$ as follows:

$$E^-(z,t) = E^+(z,t)*R^+(z,t). \tag{38}$$

The reflection data obtained from measurement can be mentioned as $E^-(0, t)$ at the first layer (Figure 9). To find the reflection kernel $R^+(0, t)$ at this layer, we have to perform a deconvolution. As a result:

$$R^+(0,t) = \text{decon}\{E^-(0,t), f(t)\} \text{ as } f(t) = E^+(0,t). \tag{39}$$

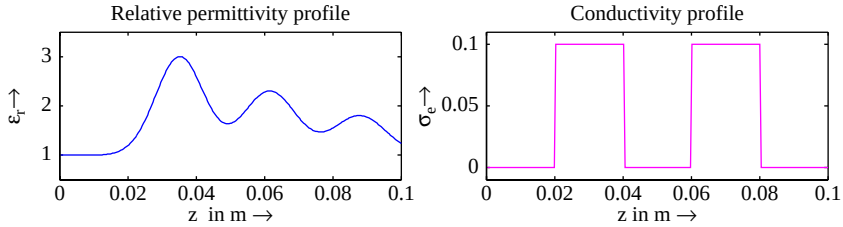

Figure 7.
Arbitrary smooth profile: ε_r (left) and σ_e (right) profile

Notes: Parameter: L = 10 cm, $N_z = N_x$ = 256, Δ = 3.9 μm, Δt = 1.7 ps

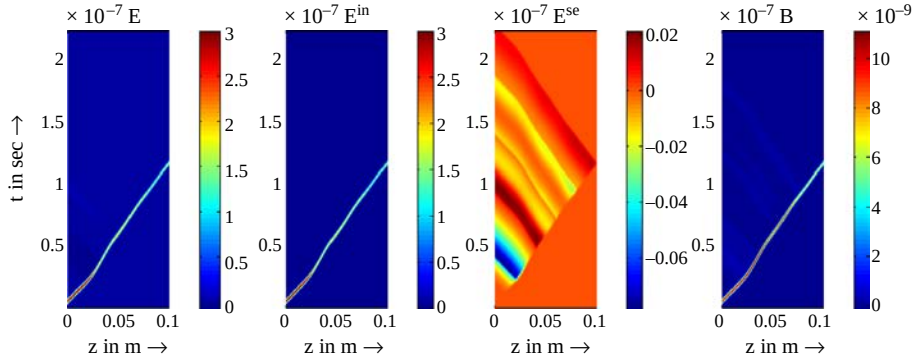

Figure 8.
Computed wave field: E: total, E^{in}: incident, and E^{sc}: scattered electric field strength as well as B: magnetic flux density

Notes: Parameter: L = 10 cm, $N_z = N_x$ = 256, Δ = 3.9 μm, Δt = 1.7 ps

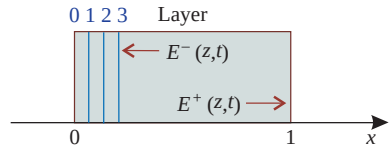

Figure 9.
Wave splitting and layer approach

As deconvolution is much easier to perform in frequency domain, the time domain parameters $f(t)$ and $E^-(0, t)$ will be transformed into frequency domain parameters $F(\omega)$ and $E^-(\omega)$ at first by using fast Fourier transform. Then in frequency domain it can be written as:

$$E^-(\omega) = R^+(\omega)F(\omega) \Rightarrow R^+(\omega) = \frac{E^-(\omega)}{F(\omega)}. \tag{40}$$

The obtained data should be filtered in order to avoid zeros which might occur at the deconvolution step. A Hanning window is used in this scheme as a filter. At the end, $R^+(\omega)$ is converted into $R^+(0, t)$ by inverse fast Fourier transform. Then the reflection data from the first layer will be used to initiate the reconstruction process.

X. Reflection kernel and reconstruction basics

Equation (38) can be rewritten as:

$$E^-(z,t) = \int_{-\infty}^{t} R^+(z, t-t')E^+(z,t')\mathrm{d}t'. \tag{41}$$

Solving this equation for $R^+(z, t)$:

$$\frac{\partial}{\partial z}R^+(z,t) - \frac{2}{c(z)}\frac{\partial}{\partial t}R^+(z,t) = \frac{c'(z)}{2c(z)}\int_0^t R^+(z,t-t')R^+(z,t')\mathrm{d}t' \tag{42}$$

$$R^+(z,0) = \frac{1}{4}c'(z) \tag{43}$$

$$R^+(L,t) = 0. \tag{44}$$

Before entering the reconstruction step, normalization will be performed according to the principle explained in Section 3. So the reflection kernel $R^+(z, t)$ will be transformed into $R^+(x, s)$ according to the relationship $R^+(x,s) = lR^+(z,t)$. Equations (42)-(44) will become:

$$\frac{\partial}{\partial x}R^+(x,s) - 2\frac{\partial}{\partial s}R^+(x,s) = -\frac{A(x)}{2}\int_0^s R^+(x,s-s')R^+(x,s')\mathrm{d}s' \tag{45}$$

$$R^+(x,0) = -\frac{1}{4}A(x) \tag{46}$$

$$R^+(1,s) = 0. \tag{47}$$

The next step is to determine the mapping parameter $z(x)$ and the permittivity profile $\varepsilon[z(x)]$. From equation (7):

$$\begin{aligned} A(x) = -\frac{\mathrm{d}}{\mathrm{d}x}\ln c[z(x)] &\Rightarrow \ln c[z(x)] = -\int_0^x A(x')\mathrm{d}x' + \text{const.} \\ &\Rightarrow c[z(x)] = k\exp\left\{-\int_0^x A(x')\mathrm{d}x'\right\}. \end{aligned} \tag{48}$$

The constant k represents $c(0)$, the phase velocity of the first layer, i.e. at $x = 0$. Now from normalization principle:

$$x(z) = \int_0^z \frac{1}{l\,c(z')}\,\mathrm{d}z' \Rightarrow \frac{\mathrm{d}}{\mathrm{d}z}\,x(z) = -\frac{1}{l\,c(z)} \quad \Rightarrow c(z(x)) = -\frac{1}{l}\,\frac{\mathrm{d}}{\mathrm{d}x}\,z(x). \tag{49}$$

From equations (48) and (49) it can be summed up that:

$$z(x) = c(0)l\int_0^x \left[\exp\left\{-\int_0^{x'} A(x'')\mathrm{d}x''\right\}\mathrm{d}x'\right]. \tag{50}$$

Replacing $c(z)$ by $1/\sqrt{\mu\varepsilon(z)}$, equation (43) can be rewritten as:

$$\frac{1}{\mu\varepsilon(z)} = \frac{1}{\mu\varepsilon(0)}\exp\left\{-2\int_0^x A(x')\mathrm{d}x'\right\} \Rightarrow \varepsilon[z(x)] = \varepsilon_1\exp\left\{2\int_0^x A(x')\mathrm{d}x'\right\}; \quad 0 < x < 1, \tag{51}$$

where $\varepsilon_1 = \varepsilon(0)$ represents the permittivity of the first layer or the first medium. Equations (50) and (51) are the basic equations for reconstruction. The transmission kernel $T^+(z, t)$, required to determine the electric conductivity σ_e profile of the unknown slab, can be associated with the forward traveling wave $E^+(z, t)$ as:

$$u^+(1, s + 1 - x) = t^+(x, 1)\left\{u^+(x, s) + \int_{s'=0}^{s} T(x, s - s'u^+(x, s')\mathrm{d}s'\right\}. \tag{52}$$

XI. Numerical implementation of the inverse solver

The embedding equation (40) can be rewritten as:

$$\frac{\partial}{\partial x}\,R^+(x, s - 2x) = -\frac{1}{2}\,A(x)\int_0^{s-2x} R^+(x, s - 2x - s')R^+(x, s')\mathrm{d}s'. \tag{53}$$

Let us fix a constant $\Delta(= \Delta x = \Delta s)$. Integrating this equation from $x-\Delta$ to x and keeping time at $s + 2x$, yields:

$$R^+(x, s) - R^+(x - \Delta, s + 2\Delta) = -\frac{1}{2}\int_{x-\Delta}^{x} A(x')(R^+ {*} R^+)(x', s + 2(x - x'))\mathrm{d}x', \tag{54}$$

where:

$$(R^+ {*} R^+)(x, s) = \int_0^s R^+(x, s - s')R^+(x, s')\mathrm{d}s'. \tag{55}$$

Let us introduce a uniform grid of points (x_i, sj):

$$x_i = i\Delta, \quad i = 0, 1, \ldots, N \text{ and } s_j = 2j\Delta, \quad j = 0, 1, \ldots, N - i. \tag{56}$$

Considering $\Delta = 1/N$, where N is the number of grid points, yields:

$$R_{i,j} = R(x_i, s_j); \quad A_i = A(x_i). \tag{57}$$

Using this grid point, equation (54) will be transformed into:

$$R_{i,j}^{+}=\left[R_{i-1,j+1}^{+}-\frac{\Delta^2}{2}\left\{A_i\sum_{k=1}^{j-1}R_{i,j-k}^{+}R_{i,k}^{+}+A_{i-1}\sum_{k=1}^{j+1}R_{i-1,j+1-k}^{+}R_{i-1,k}^{+}\right\}\right]\left(1-\frac{\Delta^2}{8}A_i^2\right). \tag{58}$$

Again from equation (46):

$$A_i=-4R_{i-1,1}^{+}\left\{1+\frac{\Delta^2}{8}A_{i-1}^2\right\}. \tag{59}$$

The error made in equations (49) and (50) is of order $O(\Delta^3)$. The initialization of the algorithm is made by assigning:

$$R_{0,j}^{+}=R^{+}(0,2j\Delta)=lR^{+}(2jl\Delta);\quad j=0,1,\ldots,N. \tag{60}$$

The reconstruction is done in two steps as shown in Figure 10. At first, $A(x_i)$ is calculated from the $(i-1)$-th grid. Second, $R_{i,j}^{+}$ is calculated from current time step data of the $(i-1)$-th grid, old time step data of the i-th grid and next time step data of the $(i-1)$-th grid.

XII. Software implementation of the inverse solver

The inversion scheme has already been tested to reconstruct sinusoidal shaped, square shaped, and multiple Gaussian shaped relative permittivity profiles using the reflection data from the Dirac pulse, the Gaussian pulse, five pulses of a sinusoidal wave, raised cosine and step function in both noisy and noise-free environments. As an example, we focus on the first test specimen considered for the forward solver and compute the profiles of the relative permittivity and electric conductivity by applying synthetic reflection and transmission data. Figure 11 shows inversion results of synthetic data.

In Figure 12 reconstruction is performed using measured data from lime sandstone, provided by the Federal Institute for Materials Research and Testing (BAM, Germany). The reference signal is a step function of the magnitude of 1 V. The measured reflected signal is shown on the left and the reconstructed relative permittivity profile is presented on the right. Lime sandstone has the relative permittivity of the range of 5-8 depending on the moisture level and the amount of impurities inside it. The test result shown in Figure 12, lies in that range and thus complies with the theoretical data.

XIII. Conclusions

The presented forward and inverse solver show accurate modeling and inversion results for different types of slabs and incident electromagnetic pulses. Slabs having continuous and discontinuous relative permittivity and electric conductivity profiles have already been tested successfully. The inverse algorithm is specially suitable for time domain reflectometry applications. Further, modifications are under development to use this algorithm for ground-penetrating radar applications.

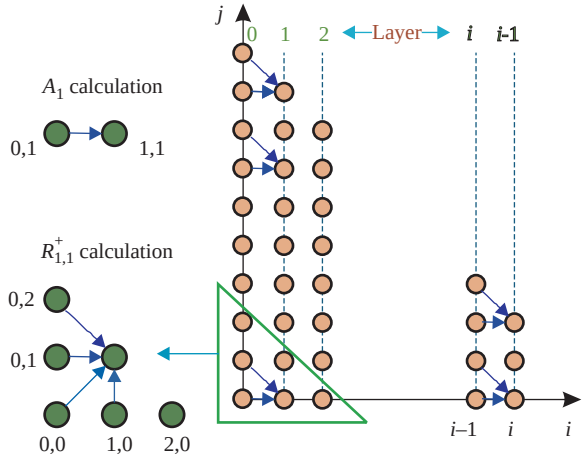

Figure 10.
Numerical algorithm of inversion scheme

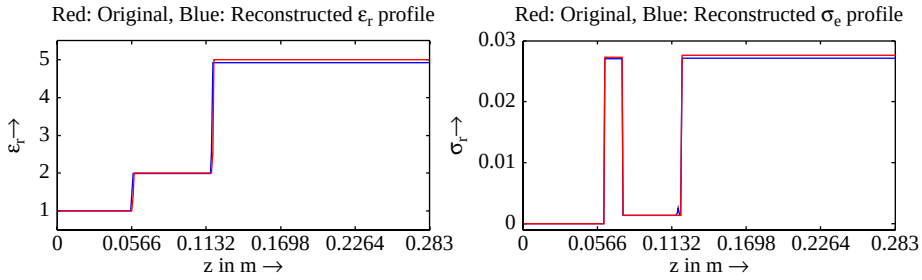

Figure 11.
Inversion results validated against the original profiles: ε_r (left) and σ_e (right)

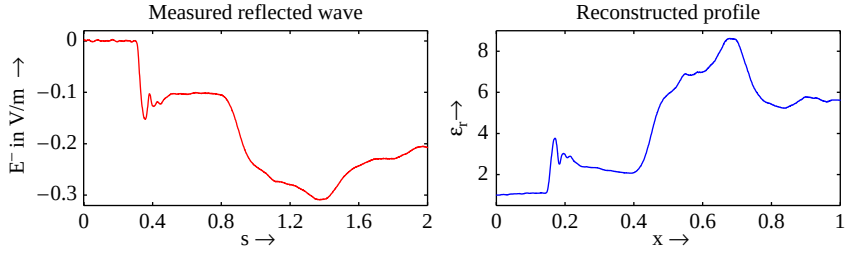

Figure 12.
Left: measured reflected wave from a lime sandstone profile, right: reconstructed ε_r profile

References

Connor, K.M. and Dowding, C.H. (1999), *GeoMeasurements by Pulsing TDR Cables and Probes*, CRC Press, Boca Raton, FL.

Corones, J.P., Davison, M.E. and Krueger, R.J. (1983), "Wave splittings, invariant imbedding and inverse scattering", *Inverse Optics, Proc. SPIE*, Vol. 413, pp. 102-6.

Jin, J. (2002), *The Finite Element Method in Electromagnetics*, Wiley, New York, NY.

Kristensson, G. and Krueger, R.J. (1986), "Direct and inverse scattering in the time domain for a dissipative wave equation, Part 1 and Part 2", *Journal of Mathematical Physics*, Vol. 27, pp. 1667-93.

Kristensson, G. and Krueger, R.J. (1992), "Time domain inversion techniques for electromagnetic scattering problems", in Corones, J.P., Kristensson, G., Nelson, P. and Seth, D.L. (Eds), *Invariant Imbedding and Inverse Problems*, SIAM, Philadelphia, PA, pp. 10-15.

Krueger, R.J. and Ochs, R.L. Jr (1989), "A Green's function approach to the determination of internal fields", *Wave Motion*, Vol. 11, pp. 525-43.

Marklein, R. (2002), "The finite integration technique as a general tool to compute acoustic, electromagnetic, elastodynamic, and coupled wave fields", in Stone, W.R. (Ed.), *Review of Radio Science: 1999-2002 URSI*, IEEE Press, Piscataway, NJ, pp. 201-44.

Rahman, M.-U. and Marklein, R. (2005), "Time-domain techniques for computation and reconstruction of one-dimensional profiles", *Advances in Radio Science*, Vol. 3, pp. 219-25.

Schlaeger, S. (2002), "Inversion of TDR measurements to reconstruct spatially distributed geophysical ground parameter", PhD thesis, Karlsruhe.

Taflove, A. and Hagness, S.C. (2000), *Computational Electrodynamics: The Finite-Difference Time-Domain Method*, 2nd ed., Artech House, Boston, MA.

Weiland, T. (1977), "A discretization method for the solution of Maxwell's equations for six-component fields", *Electronics and Communications*, Vol. 31 No. 3, pp. 116-20.

About the authors

Mehbub-ur Rahman completed the MSc degree at the Department of Electromagnetic Field Theory, University of Kassel in 2005. He is pursuing his PhD degree at the Department of Computational Electronics and Photonics (CEP), University of Kassel. His research interest lies in the numerical modeling, inverse scattering, photonics, and eddy current testing. Mehbub-ur Rahman is the corresponding author and can be contacted at: mehbub@uni-kassel.de

René Marklein is a Senior Engineer and Private Lecturer (Priv.-Doz.) in the CEP Group, Department of Electrical Engineering and Computer Science, University of Kassel, Germany. He received the BSc degree (Diploma I) in 1990, the MSc degree (Diploma II) in 1992, the PhD degree (Dr-Ing) in 1997 all in Electrical Engineering, and the Habilitation degree in 2008 from the University of Kassel, Germany. His main research interest lies in the numerical modeling, inverse scattering, and signal processing of acoustic, electromagnetic, elastodynamic fields and waves as well as coupled field and wave problems with applications in NDT, remote sensing, geophysics, electronics, and photonics.